# ABSTRACT


| | |
|---|---|
| Title of Thesis: | UTILIZING LOW TEMPERATURES TO REDUCE DEFORMATION IN 3D PRINTED HYDROGEL LATTICES |
| | Yahya Cheema, Kunal Dharmadhikari, Michael Hildreth, Neal Kewalramani, Catherine Liu, Alexi Rodriguez, Danielle Sidelnikov, Pavan Vemulakonda, Linnea Warburton |
| Thesis Directed By: | Dr. Lester Schultheis<br>Fischell Department of Bioengineering |



Patients who experience end-stage organ failure frequently require life-saving transplants. In order to mitigate the impact of the shortage, researchers have aimed to produce 3D bioprinted multi cellular constructs that can effectively replace damage organs in the human body and improve patient outcomes. Extrusion-based bioprinting is commonly used to create cell-laden lattice structures that have been implanted in animals to enhance the function of diseased organs. Extrusion-based bioprinting provides the printing resolution necessary to produce the morphological and cellular complex tissue lattices including intricate vascular channels necessary to support cell growth and proliferation. However, extrusion-based bioprinting requires the use of hydrogels with rheological properties that are such to produce stiffer tissues in order to maintain the 3D structures printer, and it is not ideal for softer tissues like brain and

lung. There is the need to develop methods that enable the bioprinting of softer tissues. Cryogenic-based bioprinting has been used as a method to bioprint soft tissues. We produced a low-temperature 3D bioprinting assembly with a Peltier platform and investigated the effect of low-temperature on bioink deformation upon deposition. A custom build platform installed into a Cellink™ Inkredible Bioprinter stabilized the implanted Peltier device and enhanced heat dissipation for the achievement of lower temperatures. We hypothesized that a reduction in deformation and collapse might increase bioprint shape fidelity and resolution. Upon initial inspection, the proof of concept studies indicated the trend that low-temperature lattices have a smaller area of deformation in comparison to room temperature lattices. Further analyses indicated no statistically significant difference between pore size and compactness of lattices printed at room and low-temperatures. Future studies should continue to analyze printing parameters and conduct identical analyses with layered lattices of significant height in which filament fusion and collapse becomes a larger concern.

# UTILIZING CRYOGENIC TEMPERATURES TO REDUCE DEFORMATION IN 3D PRINTED HYDROGEL LATTICES

By
Team
TISSUE

**Yahya Cheema**
**Kunal Dharmadhikari**
**Michael Hildreth**
**Neal Kewalramani**
**Catherine Liu**
**Alexi Rodriguez**
**Danielle Sidelnikov**
**Pavan Vemulakonda**
**Linnea Warburton**

Thesis submitted in partial fulfillment
of the requirements of the Gemstone Program
University of Maryland,
College Park
2020

Advisory Committee:
Dr. Lester Schultheis, Mentor
Dr. Martha Wang
Dr. Marc Ferrer
Cdr. James Coburn

# Acknowledgements

We would like to express our appreciation to the following individuals who helped us over the course of our research. Thank you to Dr. Lester Schultheis, our Gemstone mentor, for his guidance over the past four years. Thank you to Kevin Aroom, who advised us on 3D bioprinting. Thank you to the Terrapin Works Research Prototyping Laboratory. Thank you to Elizabeth Soergel and the University of Maryland Libraries for advising the writing of our proposal and thesis. Thank you to Adam Metzbower for helping with the design of our bioprinter print platform. Thank you to the Robert E. Fischell Institute for Biomedical Devices (Fischell Department of Bioengineering, University of Maryland, College Park, MD) for their support. Thank you to the Gemstone Program staff for their support and assistance in providing us an opportunity to conduct this research, including Dr. Frank Coale, Dr. Kristan Skendall, Dr. Leah Tobin, Vickie Hill, and Jessica Lee.

# Table of Contents

# List of Tables

# List of Figures

# 1. Introduction

Within the last few years, a novel method of manufacturing acellular and cell laden scaffolds arose in 3D bioprinting, opening new avenues for advancement in drug delivery, and regenerative medicine, disease modeling and drug screening. Unlike non-3D bioprinting methods, fused deposition modeling (FDM), a common form of 3D printing of plastics, allows for creation of complex designs, generating precise 3D architecture. Like all types of 3D printing, 3D bioprinting faces the same constraints and challenges such as printing fidelity and , and resolution stability, which will influence the final printed structure (Derakhshanfar et al., 2018), bioprinting has added complexity with the use of biocompatible materials and cell survival both through the bioprinting process and within the tissue produced. In addition to these challenges, 3D bioprinting must also overcome other constraints that extend beyond FDM printing of plastics. One such challenge 3D bioprinting faces is the low phase transition temperature of the printing fluid (Adamkiewicz & Rubinsky, 2015). Conventional 3D printers feed plastic into a print head which hovers over a print bed. From here, the printer heats the print head, melting the plastic, and then deposits the melted material onto the print bed along the XY axis according to a predetermined design. This creates one layer of deposited material, onto which the print head will print another layer, moving in the XYZ axis, layer by layer until the finalized object's creation. During this process, the molten material quickly solidifies on the print bed at room temperature, allowing an easily built upon foundation as the print escalates. This process, however, presents a major hurdle for 3D bioprinting due to the gel-like nature of many bioinks. Due to their clinical or lab use, many bioinks do not solidify at room temperature,

which over time may cause problems due to their lack of mechanical stability. Current research looks to mimic various soft tissues by utilizing the effects of cell differentiation and regeneration in 3D printed scaffolds crafted from soft bioinks (Tan et al., 2017). However, soft bioinks by definition, frequently collapse under their own weight due lack of mechanical stability. As a result, multilayer, complex architectures become difficult to print, drastically reducing resolution, and inhibiting accurate measurements (Tan et al., 2017). To correct this issue and develop more advancements in 3D bioprinting requires innovation in both bioink development, and bioprinting methods (Derakhshanfar et al. 2018). 3D printing techniques that produce mechanically and geometrically accurate scaffolds hold significant potential to create major advancements in the tissue engineering field (Tan et al., 2017).

## 2. Literature Review

### 2.1 Medical Need: Organ Shortage

Regenerative medicine applications of 3D bioprinting aim to solve the shortage of organs for transplantation. Organ transplants have long been the superior option of treatment for patients with end-stage organ failure (Shafran et al., 2014). There are many potential options for organ transplants. Xenografts represent transplants from a donor of one species to a recipient of another. One example of this would be a porcine heart valve. Allografts are transplants from donors to recipients of the same species. These transplants have much better outcomes than xenografts and result in improved quality of life. The main method of organ transplantation is through deceased donor donation, requiring prior permission from either the donor before they passed away or from the donor's next of kin, a traumatic and painful process.

Unfortunately, the increase in the number of patients who need organ transplants has far outpaced the supply of organ donations, even with these additional donor groups. The outcome is a long waiting list for transplants ("Organ Donation Statistics", 2020). In 2019, there were over 30,000 organ transplants; but every ten minutes, another patient needing a transplant was added to the waitlist (Israni et al., 2020). Moreover, patients' average waiting time can be 186 to 685 days depending on the type of organ that is required, resulting in some patients waiting for years (Bentley & Ortner, 2020).

Additionally, even after a successful transplant, organs can be susceptible to acute tissue rejection due to the uniqueness of human antigens, which can trigger robust immune responses. Lung immune rejection can, for example, be accompanied by a multitude of symptoms such as respiratory illness, shortness of breath, and death (Martinu et al., 2011). Organ rejections result in physical pain to the patient, as well as emotional trauma because the patient must enter the waiting list again and hope to get another organ transplant soon. There have been several attempts to alleviate the organ shortage crisis. These include efforts to raise awareness of deceased donor donations, advocacy for live donor donations, and increased usage of paired donor exchange (Saidi & Hejazi, 2014). There have also been new donor groups created that also have the potential to provide transplant organs. The amount of donors after circulatory death (DCD) and expanded criteria donors (ECD) have greatly increased since emphasizing their potential. However, DCDs, although more ideal, do not occur as often as deceased donors and both DCDs and ECDs result in increased rates of organ discard, often due to concerns of disease transmission (Klein et al., 2010). Clearly, human donors are not a long-term viable

solution for the organ shortage crisis. Recently, 3D-printed tissue constructs have been used to generate complex cellular scaffolds that can mimic some features of real human tissue such as cartilage and skin (Xia et al., 2018). With further research, 3D bioprinted tissues may be able to cross the hurdle of organ shortage entirely by transplanting synthetic organs into those with end-stage organ failure.

## 2.2 Tissue Engineering Approaches for Organ Regeneration

In recent years, researchers have aimed to solve issues with natural organ transplantation by producing artificial organs using tissue engineering technologies. One tissue engineering method that researchers have investigated involves seeding cells onto biocompatible scaffolds which have the ability to support proliferation and migration. Cells can form living tissues upon incorporating into physical structures and receiving biochemical cues with, for example, growth factors in the microenvironment (Derakhshanfar et al., 2018) . In order to construct viable tissues or organs *in vitro*, engineers have aimed to seed cells in biocompatible substances which can facilitate cell survival.

### *2.2.1 Cell-Based Strategies*

A challenge in the field of tissue engineering is constructing vasculature in bioprinted constructs. Tissue vasculature is significant for delivering oxygen and nutrients to cells and removing waste. Such materials can only diffuse 100-200 μm after exiting vasculature (Lovett et al., 2009). Prior studies have used a multitude of strategies to vascularize tissue *in vitro* including cell-based methods, growth factors for angiogenesis, and microfabrication of vasculature with 3D bioprinting. Cell-based methods include co-culturing a variety of

endothelial-derived cells with fibroblasts, keratinocytes, vascular smooth muscle cells, and pericytes which assist with differentiation and reinforce the structure of blood vessels. For example, in one study co-culturing endothelial cells and fibroblasts resulted in angiogenesis in 3-5 days (Min et al, 2019). Co-culturing methods have limitations for clinical applications because it is challenging to control the shape and pattern of vascular channels that result. Such methods can require a large amount of culturing time and have a high cost. Additionally, researchers have aimed to produce single-layer cells sheets which can automatically form vascular tubes after temperature-controlled detachment from the surface of a cell culturing dish. Cell-sheets have limitations with forming vasculature with the required thickness and structure to produce viable tissues (Min et al, 2019). Other cell-based methods include progressive layering which involves repeatedly injecting cells or introducing vascular structures into hosts and using their physiological machinery to regenerate tissues. This method is limited by time and feasibility for clinical application (Min et al, 2019).

*2.2.3 Cell Scaffolds*

The second class of strategies to vascularizing tissue involves using biochemical cues for angiogenesis. For example, researchers have placed vascular endothelial growth factor (VEGF), a protein which stimulates angiogenesis, within hydrogels in patterns to produce gradients which can be used to control the arrangement of blood vessels. Multiple growth factors such as VEGF, platelet-derived growth factor (PDGF), and Angiopoietin 1 have been jointly placed into cell microenvironments to further enhance the process of angiogenesis. A challenge with this strategy is organizing growth factors for the appropriate spatial and temporal effects which can

guide vascularization (Rouwkema & Khademhosseini).

### *2.2.3 Growth Factors*

Cells can be seeded into hydrogels that offer physical and/or biochemical cues to direct tissue formation. Efficacious scaffolds exhibit biocompatibility and match the porosity and mechanical properties of the tissue or organ that is damaged. Additionally, for successful integration into the host, the surface properties of engineered constructs should match those of the damaged tissue (Mabrouk et al, 2020).

Decellularized scaffolds have been produced by taking cells, DNA, and other genetic components out of native tissue. Cells are physically, chemically, or enzymatically removed in order to reduce the chances of immune rejection. After successful decellularization, the resulting scaffolds retain vasculature and physical and biochemical cues. Patients' cells can then be seeded into the scaffolds and implanted into damaged areas (Gilpin & Yang, 2017). Additionally, researchers have investigated constructing scaffolds with embedded sacrificial materials. Initial studies used materials such as stainless steel needles to act as spacers and shape vascular channels. These non-sacrificial materials do not produce complex branching structures and can damage scaffold structures upon removal. Therefore, researchers have focused on sacrificial materials which can leave behind branched, vascular channels after removal with heat or glucose. Crucially, the scalability of sacrificial templates is questionable. Moreover, if sacrificial materials are not fully removed from scaffolds they might exhibit toxicity in hosts (Min et al, 2019). Other methods of scaffolding include producing PDMS micropatterned stamps which can be used in soft lithography to construct vasculature (with less than 10 μm resolution),

and producing casts with natural tissue as templates and coating the casts with hydrogel.

### *2.1.1 Bioprinted cellular scaffolds*

While many different types of 3D bioprinters exist, the three most common types of bioprinters used to print biomaterials are inkjet, micro-extrusion, and laser assisted printing (Murphy & Atala, 2014). Printing methods are often selected based on print resolution, probability of cell viability, and preferred choice of biomaterial.

### *2.1.2 Inkjet Printing*

Inkjet, often referred to as droplet printers, deliver controlled volumes of liquid to predetermined locations. They are the most widely used 3D printing method for both biological and non biological processes. Typically, these printers contain an ink cartridge that moves about the X- and Y- axis, depositing ink on a printing surface. Inkjet printers have been successfully used to print both skin and cartilage (Cui, 2012; Skardal, 2012). The first researchers to use such printers for bioprinting modified commercial 2D printers by replacing the ink with biological materials and devising a third printhead to implement a z-axis (Murphy & Atala, 2014). Inkjet printers can be divided into two categories: thermal and acoustic. Thermal inkjet printers use heat to produce pulses of pressure that force liquid droplets from the nozzle, while acoustic inkjet printers use acoustic radiation force produced by a piezoelectric crystal actuator to eject droplets (Arslan-Yildiz, 2016).

Inkjet printers have many advantages in the process of printing biomaterials. They allow for high throughput, digital control, and the highly accurate placement of cells to the specified 2D or 3D locations by employing a layer-by-layer system of printing, allowing for 3D tissues to

be formed with complex structures (Ong et al., 2018). Systems such as nerve or vascular systems can be integrated during the tissue construction itself by allowing for gaps and channels. In addition, inkjet printers bring a higher level of ease of modification, access, and maintenance that is not available in other printers (Negro et al., 2018). It is because of these added benefits that they are commonly used among research groups involved in tissue engineering and regenerative medicine.

The bio-inks used in inkjet printing are most often water-based, which allows inkjet printers to deliver cells and biomaterials while minimizing the probability of clogging the printhead. As nozzle clogging is one of the most serious problems that researchers encounter during 3D bioprinting, this gives inkjet printers a significant advantage. By adjusting the cell or biomaterial concentration in this bio-ink, researchers can control the number of cells that are printed in each drop. For example, there is a need for such specificity in the field of quantitative cell seeding, where inkjet printers are widely used (Ong et al., 2018). These listed advantages confirm that the inkjet printing process does not greatly affect the cells that it is printing while greatly improving the 3-D printing process of tissues and cells.

### *2.1.3 Extrusion-based Printing*

The second most common type of printer for bioprinting is the micro-extrusion printer. These 3D printers contain a stage and a robotic material dispensing system, which can operate on the x, y, and z-axis. A micro-extrusion head dispenses small beads of biomaterial, rather than liquid drops, and builds the desired object in layers (Zhang & Zhang, 2015). Then, either a pneumatic or a mechanical dispenser is used to apply constant pressure and deposit the beads

(Arslan-Yildiz, 2016). The speed of deposition depends on the capabilities of the robotic motors and the diameter of the biomaterial being deposited (Lee et al., 2015). These printers can be used for many different types of biomaterials of varying viscosities and cell densities, and have been used in the past to construct aortic valves, branched vascular trees, and tumor models (Zhang & Zhang, 2015). The micro-extrusion based printer is used in bioprinting due to its ability to fabricate organized tissue constructs through a system of dispensing cells and matrix materials simultaneously (Zhao et al., 2015). Because of the ability to dispense these two materials at once, the printer is often used to repair or replace damaged tissues and organs.

A large advantage to using this printer is the ability to have spatial variations of the cells along multiple axes, which can then be used to form geometric shapes of a high complexity. The extrusion-based method of bioprinting is advantageous due to the fact that it does not require any liquid in which the target material must be dissolved in order to print. In addition, it provides ease and flexibility in handling and processing of materials, while allowing for continuous production without the need for replacing the feedstock it is using (Zhao et al., 2015).

There is currently research on the development of new polymers that can be used specifically for this style of bioprinting to help overcome the current limitations found with the current gels and their implementation with the micro-extrusion based printer and expand the window of bioprinting abilities that this printer can achieve (Ozbolat, 2017). These listed advantages confirm that the micro-extrusion based printing process has the potential to be used in a wide array of applications that it currently cannot perform in, and advance the 3-D

bioprinting process

### *2.2.7 Laser Printing*

Laser-assisted printers are less commonly used than inkjet or micro-extrusion printers, but they are beginning to be used for tissue engineering applications (Tarassoli et al., 2018). Typically, laser-assisted printers have a stage containing a layer of biological material in a liquid solution. A laser beam is then directed at a ribbon coated with laser absorbing materials such as titanium, gold, or a polyimide membrane. Following that, laser pulses are then used to create high-pressure bubbles that propel certain biomaterials towards a collector substrate (Sorkio et al., 2018). Unlike the aforementioned 3D printing methods, laser-assisted printing is a nozzleless approach.

The use of laser-assisted bioprinting comes with many advantages that result from its design and applications. For example, it has been successfully used to print cells, human dermal fibroblasts, mouse myoblasts, bovine pulmonary artery endothelial cells, breast cancer cells, and rat neural stem cells (Pati et al., 2015). Laser-assisted bioprinting employs the use of a nozzle-free, non contact process, making it more accurate and eliminating some of the room for error that is found in other printing processes. Furthermore, cells with high activity and high resolution, often at a level that is higher than those produced by other printers or other procedures, have been printed. In addition, laser-assisted bioprinting has unique control over ink droplets and precise delivery characteristics. This allows for a higher level of accuracy and control over that amount of cells being added to a print by each drop when bioprinting. Finally,

this feature of laser-assisted bioprinting eliminates the chance of failure. These listed advantages confirm that the laser-assisted bioprinting process employs unique characteristics to improve the accuracy, functionality, and the efficiency of the 3-D printing process of biomaterials. Laser printing is an undesirable method of 3D bioprinting as the high temperatures involved can cause damage to incorporated bioactive molecules (Wang et al., 2017).

## 2.2 Extrusion-based Bioprinting

Extrusion based bioprinting shows great potential for clinical use due to the controllable shape, tailored interconnectivity, and sufficient mechanical strength (Wang et al., 2017). However, it is difficult to control the surface morphology of scaffolds fabricated by existing 3D printing techniques.

### *2.2.1 Resolution*

Extrusion based Bioprinting allows for high-resolution cell deposition and accurate control over cell distribution, however the resolution is lower than other methods of printing (Mandrycky et al, 2016). Regardless, extrusion based Bioprinters are most common as most commercially available bioprinters are extrusion based, and this method has the lowest overhead cost. Extrusion based printers for non-biological purposes are capable of 5 μm and 200 μm resolution at linear speeds of 10–50 μm/s (ref. 75). Often for biological applications this resolution is lowered in an attempt to increase cell viability. For high-resolution and complex structures, the printing speed must be significantly reduced. Hinton et al. used extrusion-based 3D printing with alginate, collagen, and fibrin hydrogels and a gelatine slurry support bath to produce a resolution of ~200 μm (Tan et al., 2017).

### *2.2.2 Scale and Shape Fidelity*

One of the largest problems facing the field of 3D bioprinting is the issue of scale and shape fidelity (Ukpai et al, 2020). A serious size limitation exists for objects that are 3D bioprinted, most successful objects are only a few millimeters of a few centimeters. The underlying issue is the soft or aqueous nature of the hydrogel mixtures. These soft materials cannot support the fabrication of large structures without a significant amount of external support (Ukpai et al). The larger the 3D bioprinted structure gets, the higher the chance that it collapses under its own weight.

## 2.3 Low Temperature Bioprinting

### *2.3.1 Liquid Cooling Baths*

A promising new 3D bioprinting technique introduced by Adamkiewicz & Rubinsky (2015) and continued by Tan et al (2017), utilizes low temperatures during printing. Previous studies primarily used low temperature printing systems with liquid cooling baths. Adamkiewicz & Rubinsky (2015) used a liquid nitrogen cooling bath, and Tan et al. (2017) used carbon dioxide ($CO_2$) in an isopropanol bath. Adamkiewicz & Rubinsky (2015) modified a conventional FlashForge 3D printer to be used for bioprinting. Hydrogel was printed directly into a glass dish containing the cooling liquid while a valve controlled the level of cooling liquid. Throughout the print, the level of the cooling liquid changed continuously in order to match the height of each newly printed layer.

A potential drawback of the liquid nitrogen cooling bath designed by Adamkiewicz & Rubinsky (2015) is that the hydrogels come in direct contact with the cooling liquid. This interaction could cause issues for particular bioinks that react violently to liquid nitrogen, thereby restricting the range of usable materials for this method. Tan et al. (2017) modified this method by placing a steel plate on top of the cooling bath, and printing onto the steel plate rather than into the cooling liquid. In this method, a conventional Ultimaker 3D printer was modified for the bioprinting process. As a safer alternative to liquid nitrogen, Tan et al. (2017) utilized dry ice in an isopropanol bath. While safer than liquid nitrogen, both methods produce gas and require a readily available supply of the cooling liquid.

The primary drawback of the liquid cooling bath method is the inability to regulate and implement changes in the temperature of the print after its initiation. As described by Tan et al. (2017), a liquid cooling bath system can only produce low temperatures that are too low for optimal 3D printing (Tan et al., 2017). During printing, ice crystals form within the bioink too quickly, generating unwanted protrusions that alter the specific geometry or architecture of the print. These deformities are then amplified in the following layers, for the continuous ink flow is caught on the protrusions in the previous layer. Eventually, when the deformities become too great, the print may fail. An improved system would allow for slightly higher temperatures, which in turn will delay ice crystal formation, generating smoother layers, while still ensuring the solidification of the bioink.

### *2.3.2 Automatic Cooling Pumps*

Shi et al (2019). improved upon the liquid cooling bath design by designing a cooling stage with an automatic cooling pump. Such an approach allowed for a more constant temperature to be maintained in the set up, and allowed for more temperature control overall. The cryogenic set-up included a 3D robot platform, a pneumatic dispensing system, and a cryogenic stage (Shi et al., 2019). The automatic cooling pump had a temperature range of −80C to 99 °C ± 0.5 °C. Immediately after printing, the scaffolds were freeze-dried for 24h. After freeze-drying was complete, they were treated with a 95% ethanol solution.

*2.3.3 Cooling Platforms*

In 2017, Wang et al. modified a desktop FDM printer to contain a cryogenic stage (Wang et al., 2017). A custom cryogenic substrate at −30 °C was mounted on the printing stage and coolant was circulated. The authors successfully produced scaffolds with a desirable hierarchical porous structure. Kim et al. used a similar setup to produce 3D printed scaffolds for the regeneration of skin tissue (Kim et al., 2009). The researchers fabricated collagen scaffolds through the use of a 3D plotting system and a cryogenic refrigeration system. An injection pump, drain pump, and two compressors were used to circulate oil through the printing platform. Immediately after the printing process was completed, the scaffold was freeze-dried at −76 °C over 3 days. After freeze-drying was completed, the dried collagen scaffold was cross-linked in a 95% ethanol solution.

The processing temperature was fixed at −40 °C and the ambient temperature was fixed at 10 °C. The researchers found that at −50 °C, the collagen solution froze too quickly as it came into contact with the printing stage. Between −40 °C and −20 °C however, the collagen solution

showed good results and the dimensions of the strands were almost completely stable. However, at temperatures in this range, there appeared a difference between the diameter of the nozzle and that of the extruded collagen strands. This difference was a result of the collagen solution swelling at the nozzle tip. This "Extrudate swelling" is a common phenomenon caused by the thermal and elastic behavior of the macromolecule (Kim et al). The researchers found that this swelling decreased linearly as the temperature of the printing platform decreased. With temperatures above −10 °C, the collagen strands became slightly enlarged in diameter, and at temperatures above 0 °C, they spread out unevenly. As a result, fabrication of a 3D scaffold became impossible. With a processing temperature of −40 °C, the researchers were able to produce highly porous 3D collagen scaffolds.

## 2.4 Hydrogel Bioink

Hydrogel bioinks are cross-linked, biocompatible, hydrophilic polymers that are used in tissue engineering applications due to their ability to promote cell migration and proliferation. Bioinks can be single synthetic or natural polymers or a combination of polymers. Optimal bioinks exhibit biocompatibility, mechanical strength, and shape fidelity upon printing. They also have degradation rates similar to native tissues *in vivo*.

Common hydrogel bioinks include collagen, gelatin, fibrin, and alginate. Collagen is the most abundant protein in extracellular matrices. Collagen is biocompatible and effectively mimics the properties of tissues in the body. Collagen bioink has been 3D printed in combination with fibroblasts, keratinocytes, smooth muscle cells, and mesenchymal stem cells to produce a wide-range of tissues (Gungor-Ozkerim et al., 2018). Gelatin is produced from the hydrolysis of

collagen (Zhu & Marchant, 2011). Gelatin is an inexpensive, biocompatible polymer with RGD structures for cell binding. The polymer is less immunogenic than collagen and highly adaptable for a wide-range of applications. Fibrin is derived from fibrinogen, a protein that aids with blood clotting. The polymer is used in wound healing applications. Alginate is a biocompatible, inexpensive polysaccharide that is cross-linked with divalent cations. Alginate is advantageous because it can be modified for different applications or used in combination with other bioinks. For example, RGD motifs have been added to alginate to enhance cell growth and proliferation (Gungor-Ozkerim et al., 2018).

CELLINK™ Bioink is a commercial bioink that is composed of alginate and hydrated cellulose nanofibril. Printable bioinks must have high viscosity and good-cross linking after printing to form structures with mechanical integrity. Alginate bioinks have fast cross-linking ability, but lack the mechanical properties required for high-precision 3D printing. Alginate can be used in combination with bioinks such as cellulose with high mechanical strength. In the past, alginate and cellulose nanofibrils have been printed with chondrocytes to produce cartilage tissue (Markstedt, 2015).

### *2.5 Bioengineering vascularized tissues*

A challenge in the field of tissue engineering is constructing vasculature in bioprinted constructs. Tissue vasculature is significant for delivering oxygen and nutrients to cells and removing waste. Such materials can only diffuse 100-200 μm after exiting vasculature (Lovett et al., 2009). Prior studies have used a multitude of strategies to vascularize tissue *in vitro* including cell-based methods, growth factors for angiogenesis, and microfabrication of

vasculature with 3D bioprinting. Cell-based methods include co-culturing a variety of endothelial-derived cells with fibroblasts, keratinocytes, vascular smooth muscle cells, and pericytes which assist with differentiation and reinforce the structure of blood vessels. For example, in one study co-culturing endothelial cells and fibroblasts resulted in angiogenesis in 3-5 days (Min et al, 2019). Co-culturing methods have limitations for clinical applications because it is challenging to control the shape and pattern of vascular channels that result. Such methods can require a large amount of culturing time and have a high cost. Additionally, researchers have aimed to produce single-layer cells sheets which can automatically form vascular tubes after temperature-controlled detachment from the surface of a cell culturing dish. Cell-sheets have limitations with forming vasculature with the required thickness and structure to produce viable tissues (Min et al, 2019). Other cell-based methods include progressive layering which involves repeatedly injecting cells or introducing vascular structures into hosts and using their physiological machinery to regenerate tissues. This method is limited by time and feasibility for clinical application (Min et al, 2019).

### *2.5.1 Growth-Factors*

The second class of strategies to vascularizing tissue involves using biochemical cues for angiogenesis. For example, researchers have placed vascular endothelial growth factor (VEGF), a protein which stimulates angiogenesis, within hydrogels in patterns to produce gradients which can be used to control the arrangement of blood vessels. Multiple growth factors such as VEGF, platelet-derived growth factor (PDGF), and Angiopoietin 1 have been jointly placed into cell microenvironments to further enhance the process of angiogenesis. A challenge with this

strategy is organizing growth factors for the appropriate spatial and temporal effects which can guide vascularization (Rouwkema & Khademhosseini).

## 3. Methods

### 3.1 Printer Model and Proposed Modifications

We modified a Cellink™ Inkredible Bioprinter to accomodate for the application and adjustment of low temperatures. The Cellink™ Inkredible Bioprinter was chosen due to its ease of use, high reproducibility, and specificity. The Cellink™ Inkredible Bioprinter has been used in laboratory studies of printed skin and cartilage tissue, the main type of tissue that this project aims to print. Although skin and cartilage tissue were not printed using the Cellink™ Bioprinter, the system remained a viable option because of the printer's low cost, customizability, and print reproducibility. The body of the printer provided many opportunities for modification due to its

removable platform and side panels. With a short time frame for conducting research, the ease of use for the Cellink™ Inkredible Bioprinter improved capability for quick data collection.

In order to create a low temperature printing environment, modifications were made to the Cellink™ Inkredible Bioprinter. These modifications included removal of the side panels, inclusion of a fan and Peltier cooling device onto the build platform. The build platform itself was modified in order to accommodate the Peltier device and provide a cooling surface underneath the platform. These modifications were made in order to implement a cold printing surface for the hydrogels, as well as to constantly monitor and adjust the printing platform

temperature around a set-point temperature voltage. Further modifications were made to the printer to allow for optimal heat transfer from the cold printing platform and to provide better image resolution for print data.

The low temperature printing environment was mainly implemented through the addition of a Peltier cooling device and fan ventilation system. This system consists of the bioprinter printing onto the cooled side of the Peltier device, while the heat generated by the device accumulated and dissipated on the other side of the Peltier device through a cooling system by means of a fan.

### *3.1.1 Previous Designs Studied*

The project's overarching goal aimed to enhance the vascularity of 3D printed tissue via low-temperature 3D printing. The initial design consisted of a water cooling assembly in which a water cooling heat sink was attached to a Peltier junction with thermally conductive glue. The Peltier junction with heat sink rested on the surface of a conductive metal build platform and the water input was periodically recycled back. The second iteration included printing into a dry ice and alcohol bath. Both of the preliminary designs lacked the required fine control of temperature which is necessary for an efficacious study. In these designs, we added low-temperature modifications to a Printrbot 3D printer with a food extruder nozzle, but we found that the printer lacked the ability to produce high-resolution prints with accuracy and consistency due to limitations in printing parameters. The third iteration consisted of a temperature controlled, insulated cube structure which housed an entire 3D printer. The cube structure had an outer frame of wood and required a thermometer to measure temperature. This design, however, was

not conducive to experimentation and testing due to its bulky nature. The final series of designs focused on modifying a Cellink™ Inkredible Bioprinter with a Peltier build platform and temperature monitoring and control capabilities. Initially, the Peltier junction was placed on top of the existing build platform in the commercial bioprinter. Because the fan rested on the bottom surface of the Peltier device in contact with the build platform, the design did not allow for airflow and heat dissipation. Later, custom brackets were 3D printed and attached onto the existing build platform to elevate the Peltier junction for improved heat dissipation. In the final design, the existing build platform was replaced and a custom platform which further facilitated required heat dissipation was installed into the printer.

## 3.2 3D Printer Platform Modification

A new print platform was designed in Solidworks™ to include a hole in the middle allowing the heat from the Peltier™ device to dissipate efficiently and accommodate the Peltier size. The newly designed platform was 3D printed and screwed into the exact location of the old platform.

To replace the old print platform with the new print platform, the preexisting build plate of the Cellink™ Inkredible Bioprinter was unscrewed from the printer. The new print platform, which had the ability to be screwed in at the exact same locations on the printer, could then be properly secured to the printer. The new print platform is approximately the same size as the preexisting build plate to allow for ease of access and use when calibrating and homing the print heads. Finally, the new print bed included a pocket for the calibration switch of the Cellink™ Inkredible Bioprinter for easy

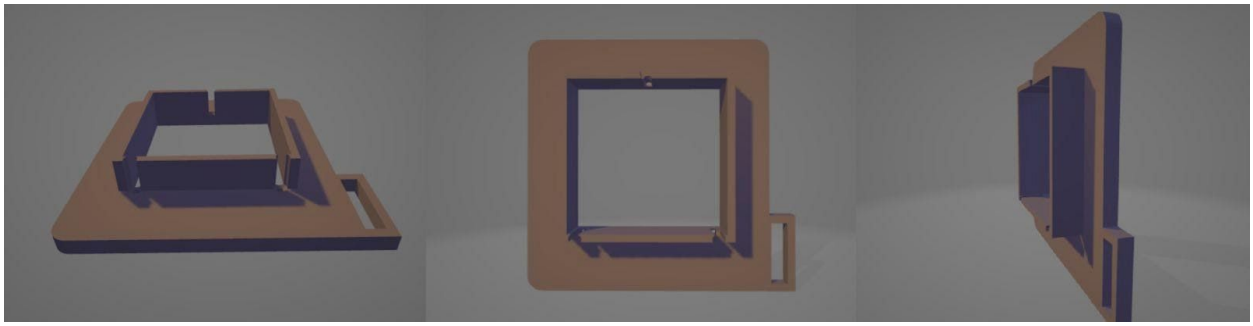

calibration. The improved build plate design is seen in Figure 3.2.1.

**Figure 3.2.1.** CAD image of improved print platform designed by Adam Metzbower to be secured in Cellink™ Inkredible Bioprinter and allowed for air flow under Peltier device while printing

## 3.3 Peltier Device Addition to Cellink™ Inkredible Bioprinter

A Peltier junction was chosen to provide a cooling printer platform surface because its temperature can be finely controlled by changing its voltage input. Within a Peltier element, N type semiconductors contain electron charge carriers while P type semiconductors contain holes, and this combination allows for the movement of charged particles, generating a cold face and hot face when current is applied.

The Laird Thermal™ DA-075-12-02-00-00 Peltier device (230 mm x 122 mm x 86 mm, 1.7 kg) was chosen for our study because of its large Peltier surface (120 mm x 60 mm x 17.90 mm) and wide temperature range.

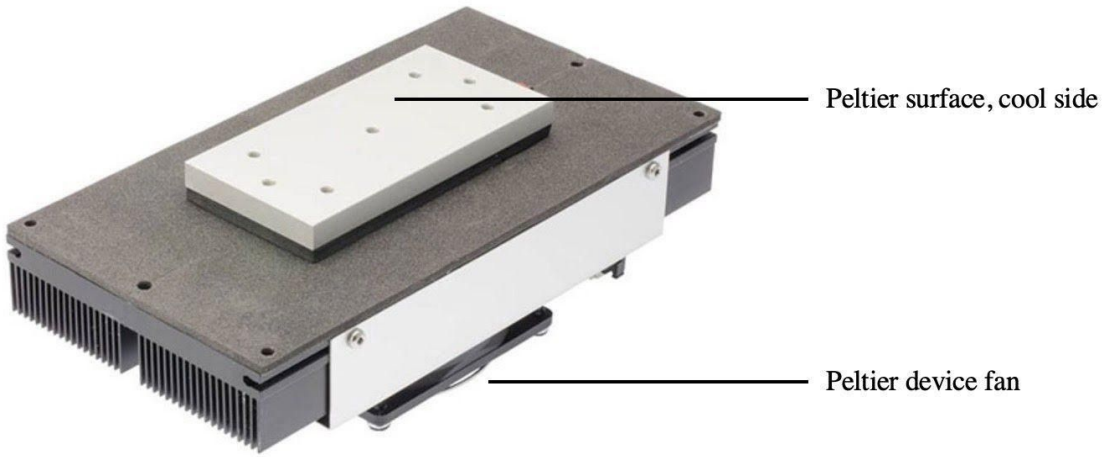


**Figure 3.3.1.** Laird Thermal™ Peltier device used in the study.

To add the Peltier device in the Cellink™ Inkredible Bioprinter, we fit its fan, which functioned to dissipate heat from the hot Peltier surface, into a lifted square component in the modified print platform (Figure 3.2.1) so that the heat sink laid on top of the roof of the modified platform. Having the fan located inside the print platform allowed for a greater printing room above the platform, which was essential for proper mobility of the 3D axis printheads.

## 3.4 Continuous Temperature Measurement System

To ensure that temperature stayed constant and at the desired temperature for low temperature prints, the temperature was tracked continuously. The temperature of the print was monitored and adjusted to oscillate around a set temperature via a predesignated voltage. The feedback loop circuit in the study was modulated by a TEC controller and involved the temperature of the Peltier system, a power source, a TEC controller, and Labview™ software as illustrated in Figure 3.4.1.

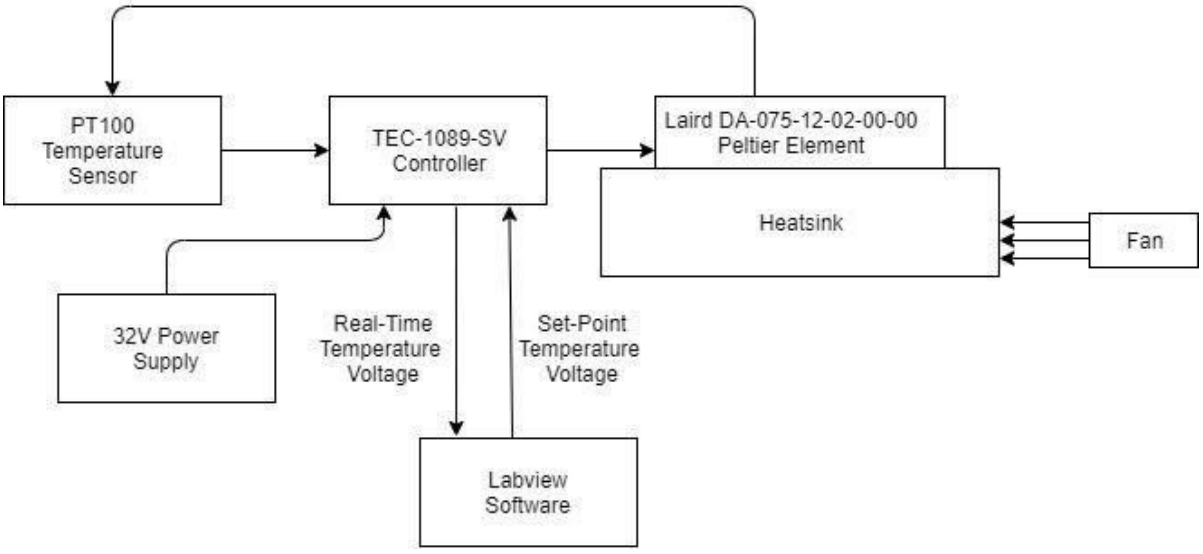


**Figure 3.4.1.** Block diagram depicting data information relationship for feedback loop of temperature regulation in the Peltier system

In the study, the Peltier device was connected to a 30-volt DC power supply to produce a stable, temperature controlled, printing surface at -26.5°C. The set point of the temperature, voltage, and amperage was determined by the user in the LabVIEW™ software. A PT100 RTD temperature sensor was used to measure the temperature of the print and the Peltier system, and this sensor was inserted into a hole drilled into the side of the aluminum housing of the Peltier surface. The sensor was secured using silver thermal conducting gel to insulate it from the external environment. Two separate temperature monitoring settings were used for the experiments. One setting involved passive temperature monitoring, which graphed temperature over a period of time to determine fluctuation. The second setting implemented active adjustments to temperature, voltage, and amperage to maintain the same amount of power flow to the Peltier, allowing for stable low temperature printing over time.

## 3.5 Bioprinting Protocol at Low and Room Temperatures

Several minutes prior to bioprinting, a 24 x 50 mm glass coverslip was placed on top of the Peltier cooling element with an attached fan which was connected to a DC power supply and allowed to reach a stable temperature of -26.5° C. Air pressure was recalibrated and set to 20 kPa for extrusion. Opaque CELLINK™ Bioink composed of alginate and hydrated cellulose was then loaded into a 3-mL deposition syringe with 24-gauge tapered plastic nozzle.

The low temperature bioprinting procedure included z-height manipulation and calibration steps to produce additional volume within the printer for the insertion of a Peltier cooling element with attached fan and temperature sensor. The deposition syringe was placed within the printer directly prior to bioprinting and removed directly after bioprinting in order to prevent clogging within the nozzle. A small quantity of bioink was extruded prior to each print in order to ensure consistency of flow. Additionally, the temperature of the Peltier element was allowed to re-stabilize to -26.5° C while in the printer. Temperature was monitored through the print to ensure variation of less than 0.5º C. For the first layer, the starting height of the tip of the nozzle was set to 0.2 mm above the surface of the Peltier cooling element (in the z-direction). For each additional layer the tip of the nozzle was positioned 0.26 mm above the preceding bioprinted layer. After the completion of a print, the hydrogel structure was allowed to rest on top of the Peltier surface for 30 seconds before the Peltier device was removed from the printer and placed within an AmScope™ MD130 light microscope and imaged with associated software. An identical procedure was used for room temperature prints except the Peltier device was not connected to a DC power supply.

## 3.6 Proof of Concept Studies

Proof of concept studies were performed to evaluate the efficacy of temperature monitoring systems and the selected printing range for various 3D printed shapes at printing resolution. After selecting the appropriate temperature monitoring system, line and lattice models were printed to test the efficacy of the modified printing system. Tests were also conducted to determine a temperature range that would reduce print deformation.

Initial testing was conducted using water equilibrated to -20ºC, 4ºC, and room temperature (25ºC). Water temperature was measured with a control thermometer (HB-Durac), laser gun (Etekcity), and a PT100 RTD temperature sensor to determine the most accurate and precise system to continually record temperature without constant researcher intervention. To test the three instruments, water was cooled to -20ºC and allowed to equilibrate to room temperature. The temperature of the water was measured over one minute intervals and compared between the three systems. This test was then performed at 4ºC and room temperature (25ºC) for a period of ten minutes.

Initial testing was conducted using temperatures of 23°C (room temperature) and -2°C. During low-temperature printing, the Peltier device was elevated 2.5 inches above the original platform of the CELLINK™ printer in order to allow for airflow. The temperature was controlled within 0.1°C electronically by negative feedback using the TEC controller. Straight lines of hydrogel were printed at 23°C and at -2°C with a 24 gauge nozzle, with fifteen lines printed for each temperature, resulting in a total of 30 lines.

Next, lattices were printed on a glass coverslip located on the cooling platform at either

-21ºC or 23ºC to compare line widths within the lattice at room temperature and low temperatures. The nanocellulose-based CELLINK™ START hydrogel was extruded through a 5 mL syringe at 0.0030 ml/s through a 24 gauge metal nozzle attached at the end. Images of each lattice were taken with a microscope and analyzed with NIH ImageJ. The area of the largest pore of the lattice was measured using NIH ImageJ for each of the printed lattices. The line width was sampled in three places along each segment and the radius of curvature was sampled at the lower outer corners. The total variation between the line widths of segments was compared for the entire lattice at -21ºC and 23ºC. The radius of the curvature of the outer corners of the lattices was measured in order to determine the amount of diffusion and fusion occurring at the corners.

## 3.7 Pivotal Study

After proof-of-concept experiments were performed, a pivotal study that was composed of a larger dataset and more comprehensive analysis was carried out. This experiment required the construction of a 3-layered lattice to determine the effect of low temperature on pore area and pore compactness and a deformation test for analysis at two temperatures.

### *3.7.1 Theoretical 3D Lattice Print*

A predictive 3D print 3-layered model lattice was constructed. Each layer was a square 12 mm x 12 mm nine-pore lattice (Figure 3.2.3) with parameters listed in Figure 3.2.4 and

implemented using G-code, a computer language that allowed for full control of the printer's actions.

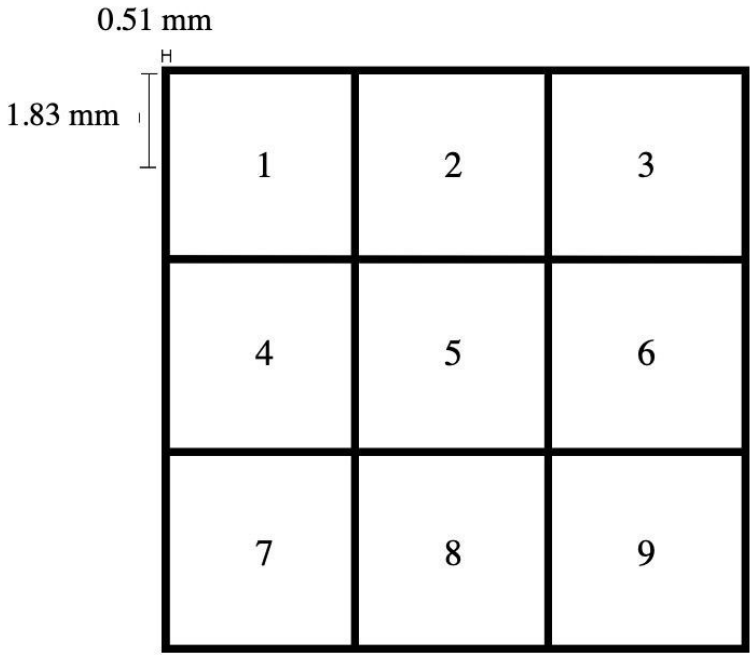


**Figure 3.4.1.** Theoretical lattice coded from G code. To distinguish pores from one another for data analysis, each pore was assigned a number.

| Parameter | Value |
|---|---|
| Wall thickness | 0.51 mm |
| Number of pores in a row | 3 |
| Number of pores per set | 9 |
| Radius of pore 1 | 1.83 mm |
| Spacing between centers of adjacent pores | 4.17 mm |

**Figure 3.4.2.** Parameters for theoretical lattice coded from G code.

*3.7.2 Deformation Testing*

A deformation test was conducted to determine if lattices printed at low temperatures maintained their shape and structure better over time compared to lattices printed at room temperature. A limited number of lattices were imaged with AmScope™ MD130 light microscope immediately after being printed (t=0), and reimaged with the microscope at the same position after five minutes at room temperature (t=5). To determine if low temperature reduced print deformation, ImageJ was used to measure the area and calculate the compactness at t=0 and t=5 of individual pores within each lattice.

Area analysis was chosen as a parameter for comparison between low and room temperature printing to quantify lattice resolution. The analysis was done using ImageJ. For each of the nine squares in the print, the "Polygon" tool was used to measure the amount of pixels in each area, excluding the actual gel component of the lattice. Each of these nine areas were normalized to the area of the entire lattice by dividing the pore area by the total lattice area. The order in which the lattices were measured was by each row, starting closest to the microscope neck. This was done by starting with the top left pore and proceeding right. These ratios were used in statistical analysis.

Compactness of each pore was analyzed to determine the circularity of a pore. To do so, area and perimeter measurements of each open pore were obtained using ImageJ by outlining the pore with the "Polygon" tool. The following formula was used to determine the compactness of a pore:

$$Compactness = \frac{4\pi * area}{perimeter^2}$$

Equation 1. Formula depicting the analysis of compactness of the corners around a pore in a lattice

the maximum value of compactness is 1, which represents a circle, the most compact shape in existence. The closer the object's compactness value is to 1, the close the shape is to a circle. The purpose of measuring compactness was to evaluate the roundness of the corners. A shape containing round corners that deviated from the original square designated by the G-code would possess a higher compactness value. A higher compactness value would indicate more deformation.

## 3.8 Statistical Analysis

The following statistical analysis tests were used to determine if there was a significant difference between both low temperature prints and room temperature prints, as well as if structural deformation was localized to specific areas in the lattice.

### *3.8.1 Analysis Between Room and Low Temperatures*

**F-Test**

An F-test was used to test if the variances of the two temperature populations are equal. The results of the F-test would determine whether to use unequal or equal variances for the following two-sample T-test. The F-value, calculated by dividing the variance of one population by the population of the other population, was compared to two critical values. If outside the range of the critical values, the null hypothesis was rejected and the two population variances were determined to be unequal.

T**wo-sample T-test**

A two-tailed T-test was performed to look for a significant difference between the room

temperature and low temperature prints, as well as information on printing consistency when reconstructing the G-code input.

To obtain information on printer consistency when reconstructing G-code input, a specific preset g-code value for total area within the pore was correlated to each square pore of the print. Based on this, a two-sample T-test was performed with a Bonferroni correction applied to each of the nine pores. This allowed for multi-comparison testing, while accounting for a possible Type I error.

The two-sample T-test was used to determine whether the means from the room and low temperature prints are statistically significant. Equal or unequal variances were assumed by running an F-test with a significance level of 0.05. The t-value calculated by dividing the difference of the sample mean and the hypothesized population mean by the quantity of the standard deviation divided by the sample size was compared to a threshold value, which varied by sample size, significance level, and whether the test was one-tailed or two-tailed. The null hypothesis stated that there was no statistical difference between the two population means. If greater than the critical value, the null hypothesis would be rejected and the two population means were stated to be significantly different at a significance level of 0.05.

### *3.8.2 Analysis of Investigator Bias*

Image analysis performed through ImageJ was carried out by nine independent investigators. Each investigator analyzed the full image set and obtained their own data for

compactness and area size. Each set of data was normalized to its own values, entirely independent from other investigators. To evaluate the presence of bias between the analyses of individual investigators, a Student's test as well as an ANOVA test was performed.

### Student's Bias Test

The bias test consisted of removing a particular researcher's data set from the entire data set, examining if there was a statistical difference in the data when this data set was removed, and then repeating the process for all researchers who provided data sets. The null hypothesis stated that the two data sets were not statistically different from one another. If outside the range of the critical values, the null hypothesis was rejected and the two separate values were stated to be significantly different. We rejected the null hypothesis for four of the nine data sets that were observed.

### ANOVA Test

An ANOVA test was used in comparison to a Student's bias test due to the multiple conditions that were compared in the experiments conducted. Potential sources of bias existed due to the qualitative manner in which 9 individual investigators obtained numerical data. This bias was mitigated by conducting a sensitivity analysis which aimed to isolate each individual's data and examine its statistical difference from the overall data set. By concluding that none of the individuals' data set was an outlier or skewed the data in any particular manner, the bias was mitigated.

### *3.8.3 Analysis of Pore Location Bias*

The theoretical 3D lattice design involved nine pores of the same size. Due to lag in the 3D printer and drag caused by the nature of the hydrogel at the start and between new columns and layers, pore sizes inevitably differed within the lattice. Leveling and other manufacturing characteristics of the 3D bioprinter may have also impacted individual pore size. Each individual pore size remained consistent between several lattices. However, statistical analysis was performed to determine significance between the sizes of pores within one lattice based on location within the print platform. This was used to determine whether these differences in pore size had a significant effect on the average pore size for the entire lattice.

#### ANOVA Test

A one-way ANOVA test was run to examine whether pore location caused inherent bias in area measurements taken in ImageJ. After running an ANOVA test in Excel for both room temperature and low temperature printing, a significant difference was found between the pores. While this does not indicate which pore might cause the bias, this does indicate that the printer's ability to reproduce the theoretical Gcode causes inherent bias when measuring the pore area.

# 4. Results

## 4.1 Proof of Concept Studies

Initial proof of concept testing involved evaluation of temperature measurement systems and selection of appropriate low temperatures through analysis of 3D printed shapes and

widths. The temperature measurement equipment was assessed to ensure the PT100 RTD could accurately, precisely, and continuously measure temperature. Various temperatures below 0°C were investigated in order to identify the ideal temperature range for low-temperature 3D printing. Evaluation of 3D printed lines and lattices allowed for selective analysis for deformation testing through quantification of line width and area of a specific pore.

After comparing the temperature measured by a control thermometer (HB-Durac), laser gun (Etekcity), and the PT100 RTD temperature sensor, it was observed that temperature measured by the control thermometer (HB-Durac) and the PT100 RTD were not found to be statistically significant ($p=0.1182$), suggesting that the PT100 RTD allowed for accurate measurements, without requiring continual monitoring by a human investigator.

Straight lines of hydrogel were printed at room temperature and at -2°C with a 24 gauge nozzle, with fifteen lines printed for each temperature. The 15 lines printed at -2°C did not display a statistically significant quantitative difference in line width compared to lines printed at 23°C (Figures 4.1.1 & 4.1.2).

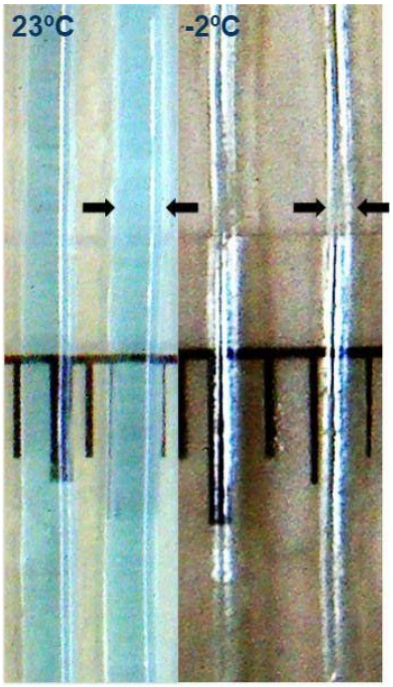


**Figure 4.1.1**. Lines printed at -2ºC and 23ºC.

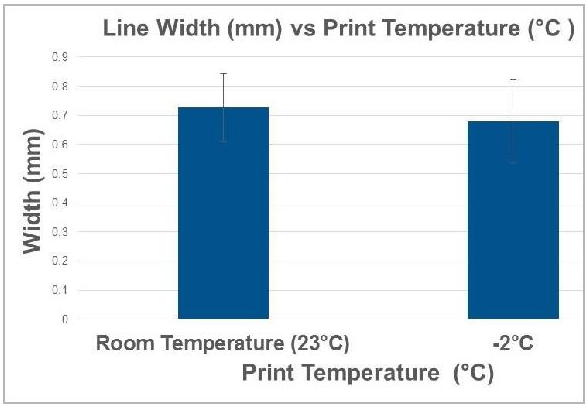


**Figure 4.1.2**. Line width (mm) variation in lines printed at -2ºC and 23ºC.

Next, an experiment involving line widths within five-layer lattices was performed and subsequently analyzed. During the printing process for the five-layer lattices, the hydrogel at room temperature often dragged and stuck to various areas of the lattice. This phenomenon resulted in large deformations or “holes” in each layer of the lattice. As the layers continued,

these deformations were magnified as the next layer of hydrogel collapsed due to the deformed support layer below.

Images of the five-layer lattices were analyzed in ImageJ to determine the area of the largest opening in the lattice pattern. Due to the large deformation that occurred during room temperature printing, quantitative analysis demonstrated that the lattices printed at low temperature had much smaller areas of deformation. Further statistical analyses proved statistical significance between these low-temperature and room-temperature prints.

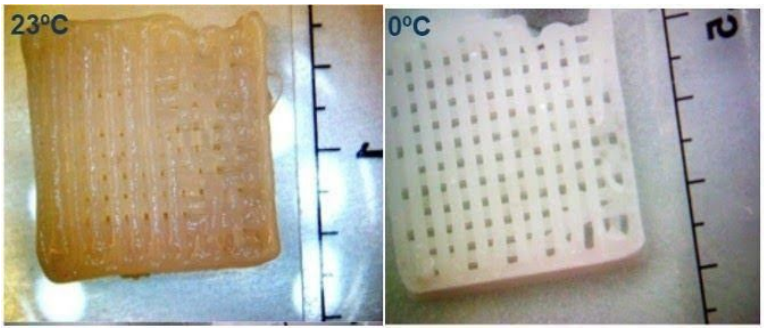


**Figure 4.1.3.** Five-layer lattices printed at 23ºC and 0ºC.

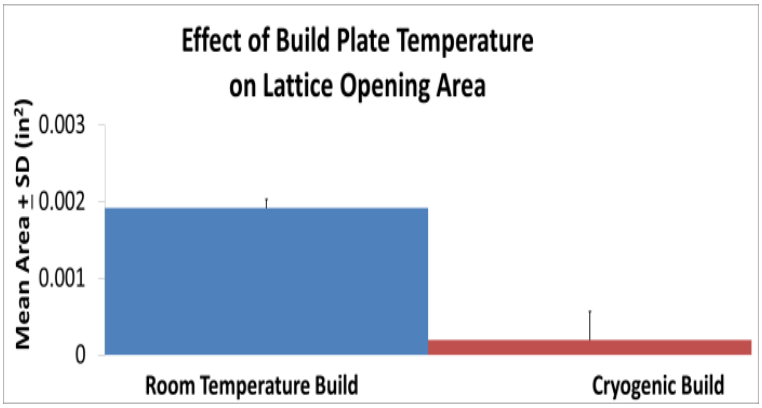


**Figure 4.1.4.** The mean lattice area at room temperature was $1.93*10^{-3}$ $mm^2$ and the mean lattice area at low-temperatures was $1.962*10^{-4}$ $mm^2$. A one-tailed T-test confirmed a statistically significant difference in lattice areas ($p<0.5$).

Lattices were printed on a glass coverslip located on the cooling platform at either -21ºC or 23ºC. The line width was sampled in three places along each segment and the radius of

curvature was sampled at the lower outer corners. The total variation between the line widths of segments was compared for the entire lattice at -21ºC and 23ºC. The radius of the curvature of the outer corners of the lattices was measured in order to determine the amount of diffusion and fusion occurring at the corners. Variation in line width was found to be lower for low-temperature prints. Statistical analyses concluded that there was no statistically significant difference between room-temperature and low-temperature prints. Analysis of the radius of the curvature between the two temperature populations demonstrated that the low-temperature prints had sharper corners but proved to be statistically insignificant between the two populations as well.

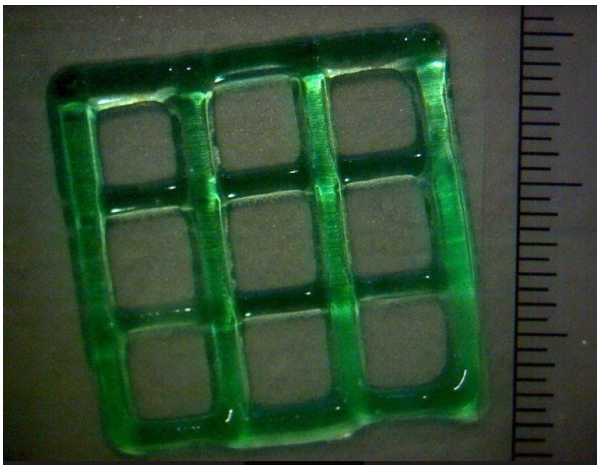

**Figure 4.1.5.** A multilayer 24mm x 24mm hydrogel lattice printed at -21°C. A line used in ImageJ to determine line width is visible on the right-hand side and middle row of the lattice.

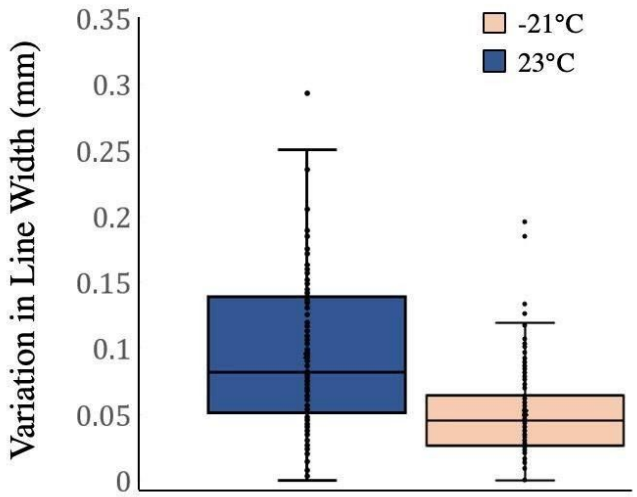


**Figure 4.1.6.** Variation of line width in the segments of lattices printed at 23°C and -21°C. Lattices printed at low temperatures display less variation in line width. Statistical analysis performed using students t test.

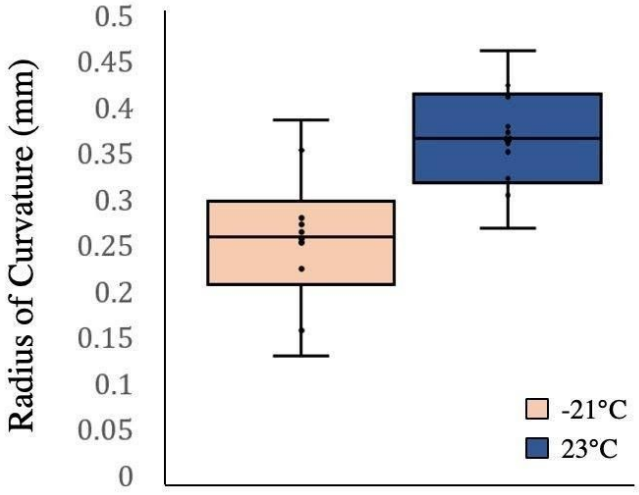


**Figure 4.1.7.** Radius of curvature of the outer corners of lattices printed at 23°C and -21°C. Lattices printed at low temperatures display less corner diffusion and fusion and thus sharper corners. Statistical analysis performed using students t test.

## 4.2 Pivotal Study

### *4.2.1 Deformation Testing*

Deformation testing results are inconclusive due to the limited number of low and room

temperature samples analyzed over time. Five minutes after printing, room temperature samples exhibited observable deformation of the structure and a decrease in pore area, while the low sample had qualitatively less deformation and changes in pore area.

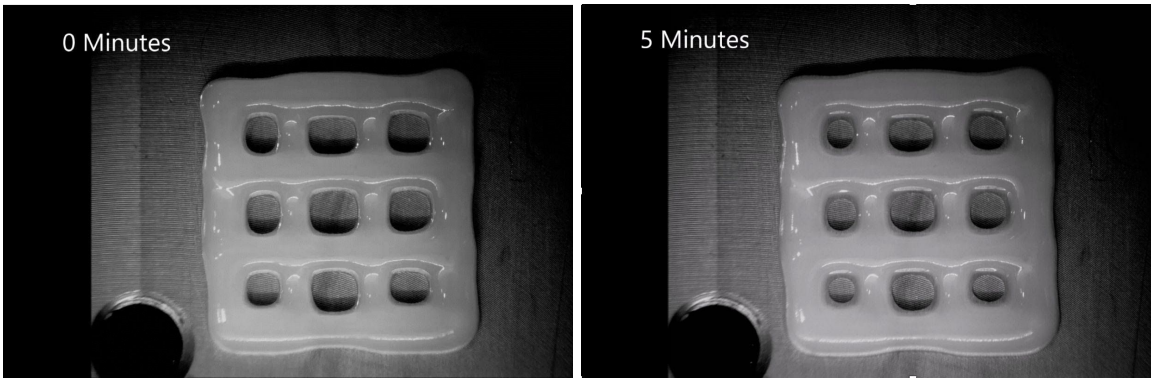


**Figure 4.2.1.** Degradation of room temperature lattice after 5 minutes

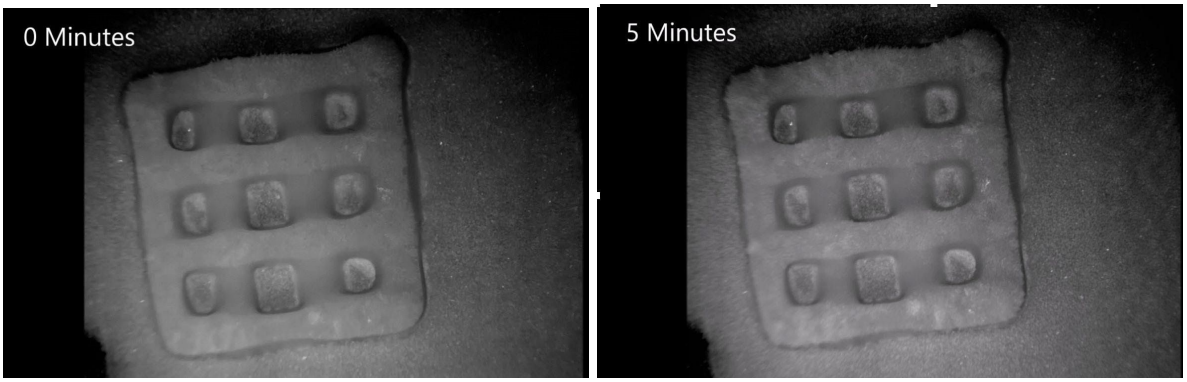


**Figure 4.2.2.** Degradation of low temperature lattice after 5 minutes

*4.2.2 Low Temperature Printing Effect On Pore Area*

Average normalized pore area is significant because it reveals the fraction of the total area of the hydrogel filament. The area contribution of hydrogel is indicative of the width of lines in the lattice structure with area and line width having a direct relationship. A larger area contribution of hydrogel that is statistically significant indicates a larger line width. Quantitative analysis in ImageJ demonstrated that while there was significant overlap in the distribution of normalized pore areas between the two groups, there was no statistically significant reduction

in normalized pore areas (area of single pore divided by total area of lattice) among the low temperature prints compared to the room temperature prints (p=.05). The distribution of normalized pore area values also varied significantly more for the room temperature group.

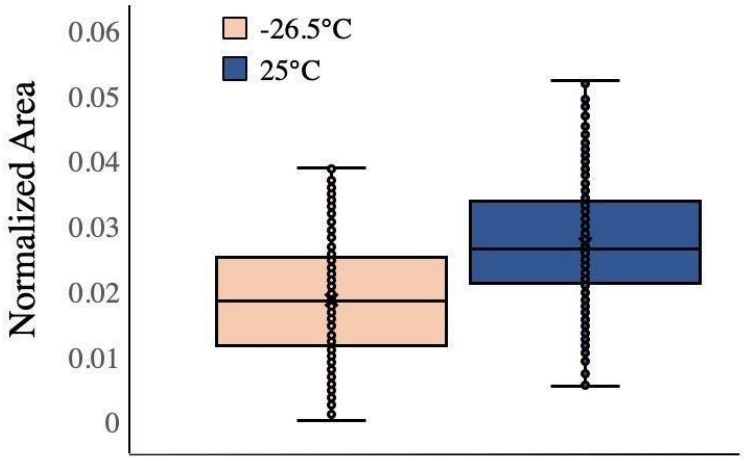


**Figure 4.2.3.** Normalized area of all 9 pores in 30 hydrogel lattices printed at -26.5ºC (n=270) and 25ºC (n=270). Each lattice was imaged within a few minutes of being printed using an AmScope MD130 microscope. 7 individuals calculated each pore's normalized area separately using ImageJ measurements.

Normalized pore area is measured by seven individuals in order to mitigate the effects of bias in interpreting detailed image characteristics. Averaging the normalized pore areas in a single lattice, it is evident that the largest pore openings were found in the room temperature treatment group. The normalized pore area values for the room temperature treatment group also varied more than the normalized pore area values for the low temperature treatment group.

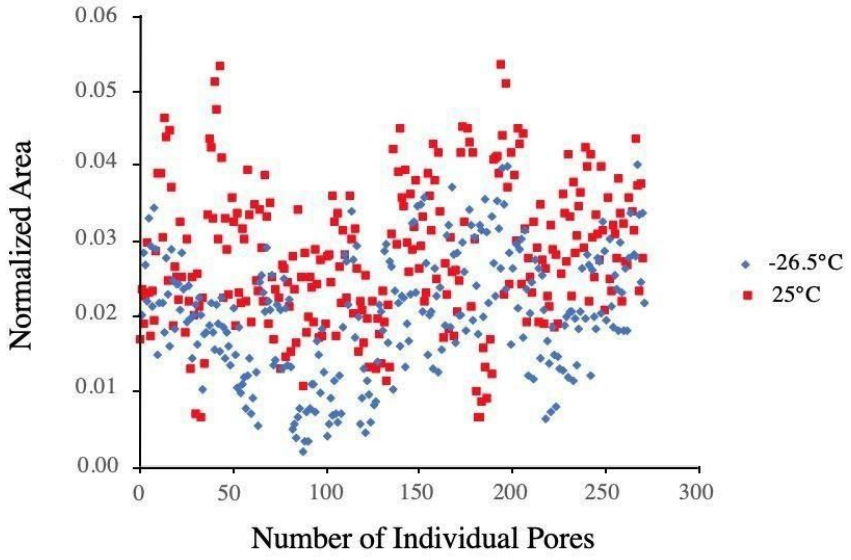


**Figure 4.2.4.** Averaged normalized area values were obtained for each pore in a 9-pore hydrogel lattice printed at -26.5ºC (n=30) and 25ºC (n=30). Each lattice was imaged right after being printed using an AmScope MD130 microscope. The normalized area of each pore was calculated using ImageJ.

For each pore within a 9-pore lattice, pore openings were larger in the room temperature lattices. Furthermore, pores 1, 4, and 7 (Figure 4.2.5), which are located on the left side of all lattices, had the smallest openings when printed at low temperatures and room temperatures.

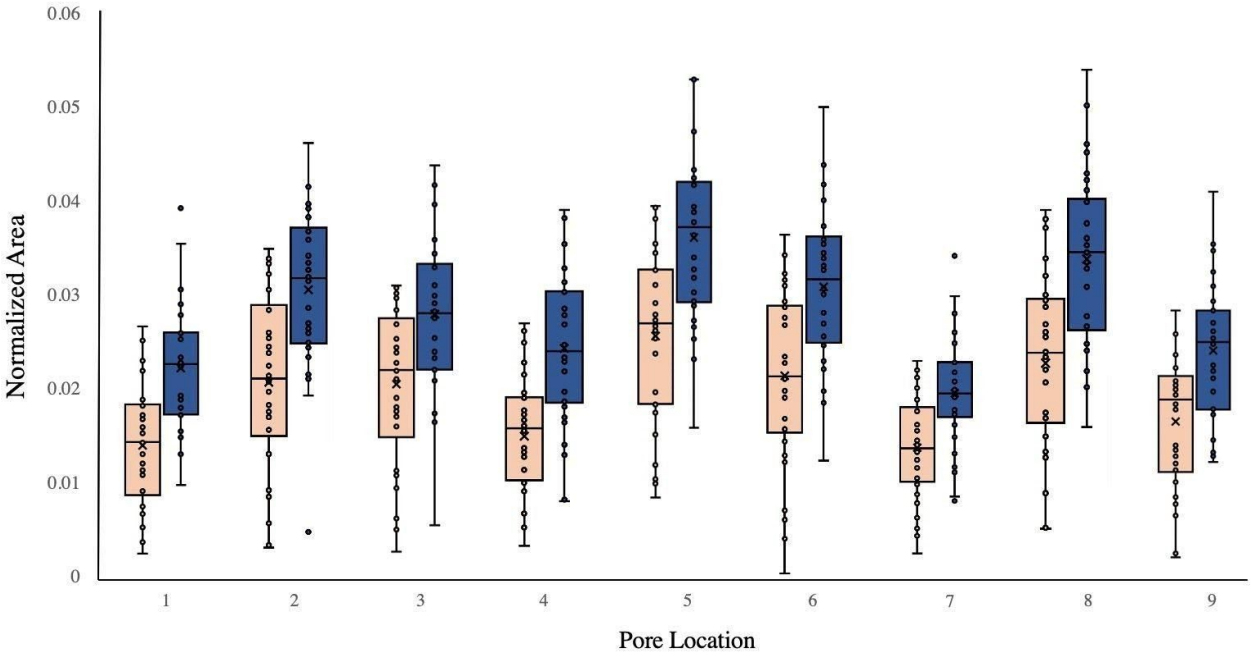


**Figure 4.2.5.** Plot demonstrating the distribution and averaged normalized pore area values obtained by 7

individuals for each pore in a 9-pore hydrogel lattice printed at -26.5ºC (n=30) or 25ºC (n=30). Each lattice was imaged right after being printed using an AmScope MD130 microscope. The normalized area of each pore was calculated using ImageJ measurements.

### *4.2.3 Low Temperature Printing Effect On Pore Shape*

While there was significant overlap present between the two groups, we found that there was no statistically significant reduction in compactness among the low temperature (-26.5ºC) prints and the room temperature (25ºC) prints, thus preventing any definitive implications or conclusions to be drawn from this data set. The presence of a more narrow distribution in calculated compactness values among low temperature prints compared to the room temperature prints, could suggest that printing at low temperature increases structural integrity and structural uniformity among prints. However, this is not confirmed through the statistical analysis conducted.

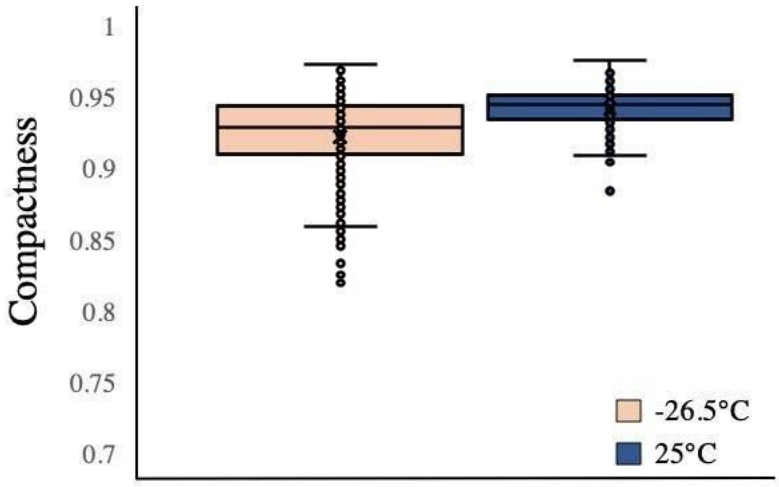


**Figure 4.2.6.** Compactness of all 9 pores in 30 hydrogel lattices printed at -26.5ºC (n=270) and 25ºC (n=270). Each lattice was imaged right after being printed using an AmScope MD130 microscope. 8 individuals calculated each pore's compactness using ImageJ measurements.

Quantitative analysis in ImageJ demonstrated that there was significant overlap in compactness between the two groups, thus illuminating further how the two groups did not differ

from each other in a statistically significant manner. The distribution of compactness values varied more for the low temperature group and while the distribution was greater, the values never exceeded that of room temperature prints.

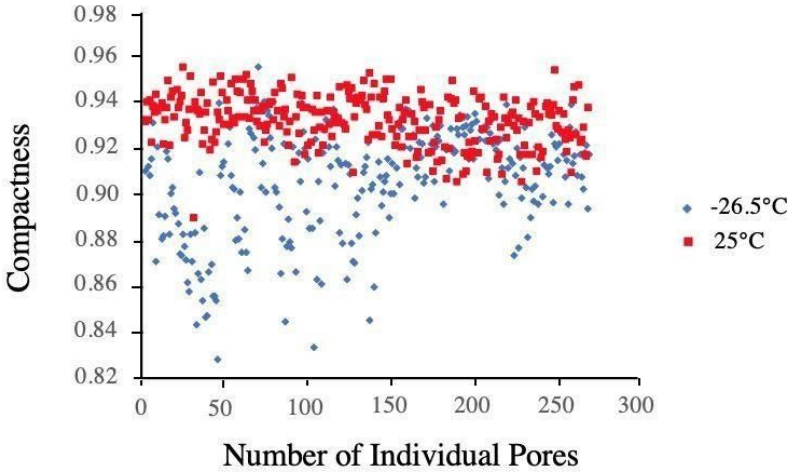


**Figure 4.2.7.** The compactness value for each pore in a nine pore lattice was measured by nine individuals. The average compactness was taken and plotted. The lattices were printed at -26.5ºC (n=30) or 25ºC (n=30). Each pore was imaged right after being printed using an AmScope MD130 microscope. The compactness of each pore was calculated using ImageJ measurements.

At each pore within a 9-pore lattice, pore openings were observed to be more compact, or circularly shaped, in the room temperature lattices. This finding was later confirmed to not have any statistical validation.

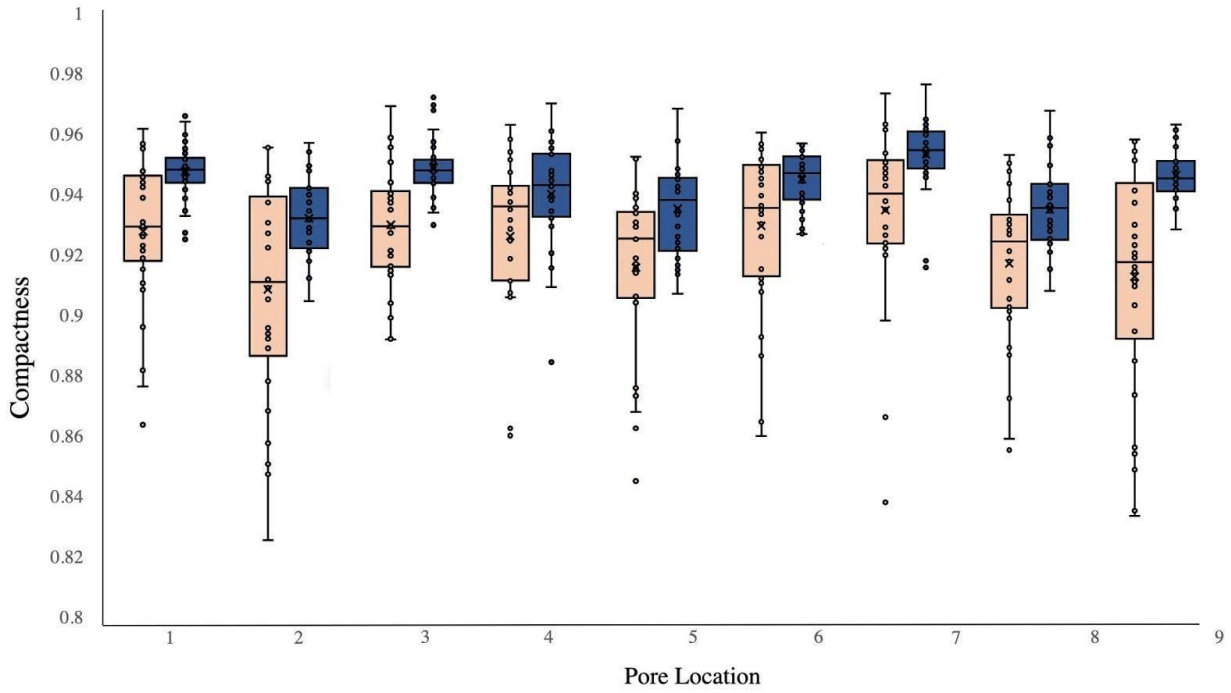


**Figure 4.2.8.** Plot demonstrating the distribution and averaged compactness values of each pore in a 9-pore hydrogel lattice printed at -26ºC (n=30) or 25ºC (n=30) obtained by 9 different individuals . Each lattice was imaged right after being printed using an AmScope MD130 microscope. The compactness of each pore was calculated using ImageJ measurements to create a ratio.

# 5. Discussion

It was anticipated that there would be a statistically significant difference between 3D printing on a low-temperature platform vs a platform at room temperature temperature based upon findings from our feasibility studies of small data sets. Among some prints, there appeared to be a compelling difference in the line width of the prints made at low temperature compared to those at room temperature. As can be seen in Figure (4.1.1), the line printed at low-temperatures is thinner than the line printed at room temperature. Therefore, the resolution of 5 layer lattices with an abundance of pores and 0.05 mm lines were analyzed. The proof of concept studies confirmed a repeatable process for analyzing images with NIH ImageJ. Additionally, room

temperature lattices in proof of concept studies had a lesser quality with regards to shape deformation and collapse in comparison to low-temperature lattices. A lattice structure shape is widely printed and used as scaffolding for cell proliferation and differentiation. The lattices used in initial studies were refined to have a larger pore area and less layers to enhance the accuracy of measurements. Additionally, these studies highlighted limitations in controlling a few variables in the printing process. Pressure and flow rate calibrations and initial nozzle distance above the build plate required finer control to have consistent extrusion of prints.

From these conclusions, we decided to proceed by comparing low-temperature prints vs room temperature prints with criteria specified in the literature. Our criteria included curvature of the pores, compactness/pore shape, and pore size of each 3x3 lattice.

Although the initial findings were promising, as a large number of prints were evaluated in our pivotal study, improvement in print quality associated with low temperature was dwarfed by other process parameters that were not fully controlled. Some of these factors include the starting height of the print head nozzle, temperature of the print head, temperature of the enclosed area within the printer, and flow rate of the pressure head. Because of these confounding variables, a statistical difference could not be demonstrated between low-temperature prints and room temperature prints based on the criteria mentioned.

After our statistical comparison of parameters of print geometry associated with print temperature, we evaluated features of our methodology that were not controlled in order to understand how they affected the quality of our prints. Ongoing work investigates the effect of

low-temperature printing on thicker print geometries, the effect of nozzle diameter, the effect of nozzle flow rate, and the effect of nozzle temperature. We concluded that subtle changes in a wide range of print process controls may affect print resolution in hydrogels. These controls include the temperature of the build platform, the temperature of the extrusion nozzle, and the extrusion flow rate. In addition, we determined that large datasets of 3D prints must be evaluated to capture the treatment effects of various changes in print process parameters.

With a Peltier device along with a temperature controller, a system with a feedback loop was designed to hold stable at -26.5℃ and 25℃. This system can be recreated with the equipment described above to replicate the experiment. In addition, the experiment can be repeated with the lattice structure used in this experiment or a new design can be implemented to test for new features. However, there were some parameters that were not controlled in this experiment such as the height of the printing nozzle, the temperature of the print head, and the temperature of the enclosed environment of the printer, which contributed to experimental variability.

## 6. Conclusion

Preliminary data suggested the effects low temperature 3D bioprinting would greatly impact and improve normal bioprinting measures. Initial findings displayed a correlation between theory and reality, with quick freezing, maintenance of print as layer height increased, and lack of deformation over a period of time. These findings suggested that low temperature 3D bioprinting could serve as a method to facilitate more precise bioprinting in the future. Despite these initial

findings, after completion of data collection, our pivotal study displayed a positive trend, but did not demonstrate statistically significant differences in lattice opening geometries associated with platform temperature. Additionally, there were no statistically significant differences between room temperature and low temperature with room temperature prints maintaining more compact pore size. Other qualitative observations were also informative. For example, low temperature printed hydrogels did not deform as quickly as did room temperature prints. Further studies are needed to further evaluate and refine low temperature 3D print technology. Future work may enable higher fidelity when printing multiple hydrogel layers with improvements in fabrication process controls.

## 7. References


Adamkiewicz, M. & B. Rubinsky (2015) low 3D printing for tissue engineering. *Cryobiology,* 71**,** 518-521.

Arslan-Yildiz, A., El Assal, R., Chen, P., Guven, S., Inci, F., & Demirci, U. (2016). Towards artificial tissue models: past, present, and future of 3D bioprinting. Biofabrication, 8(1), 014103.

Bentley, T. S., & Ortner, N. (2020). *2020 U.S. organ and tissue transplants: Cost estimates, discussion, and emerging issues* (Milliman Research Report). Milliman Inc.

Cui, X., Boland, T., De lima, D., & Lotz, M. K. (2012). Thermal Inkjet Printing in Tissue Engineering and Regenerative Medicine. *Recent Patents on Drug Delivery & Formulation, 6*(2), 149-155. doi:10.2174/187221112800672949

Derakhshanfar, S., R. Mbeleck, K. Xu, X. Zhang, W. Zhong & M. Xing (2018) 3D bioprinting for biomedical devices and tissue engineering: A review of recent trends and advances. *Bioactive Materials,* 3**,** 144-156. https://doi.org/10.1016/j.bioactmat.2017.11.008

Gilpin, A., & Yang, Y. (2017). Decellularization Strategies for Regenerative Medicine: From Processing Techniques to Applications. *BioMed Research International*, *2017*, 9831534. https://doi.org/10.1155/2017/9831534

Gungor-Ozkerim, P. S., , Inci, I., , Zhang, Y. S., , Khademhosseini, A., , & Dokmeci, M. R., (2018). Bioinks for 3D bioprinting: an overview. *Biomaterials science*, *6*(5), 915–946. https://doi.org/10.1039/c7bm00765e

Israni, A. K., Zaun, D., Hadley, N., Rosendale, J. D., Schaffhausen, C., McKinney, W., Snyder,

J. J., & Kasiske, B. L. (2020). OPTN/SRTR 2018 Annual Data Report: Deceased Organ Donation. *American Journal of Transplantation*, *20*(s1), 509–541. https://doi.org/10.1111/ajt.15678

Kim, G., Ahn, S., Yoon, H., Kim, Y., & Chun, W. (2009). A cryogenic direct-plotting system for fabrication of 3D collagen scaffolds for tissue engineering. Journal of Materials Chemistry, 19(46), 8817-8823.

Klein, A. S., Messersmith, E. E., Ratner, L. E., Kochik, R., Baliga, P. K., & Ojo, A. O. (2010). Organ Donation and Utilization in the United States, 1999–2008. *American Journal of Transplantation*, *10*(4p2), 973–986. https://doi.org/10.1111/j.1600-6143.2009.03008.x

Lee, V. K., Dias, A., Ozturk, M. S., Chen, K., Tricomi, B., Corr, D. T., Intes, X., & Dai, G. (2015). 3D Bioprinting and 3D Imaging for Stem Cell Engineering. In K. Turksen (Ed.), B*ioprinting in Regenerative Medicine* (pp. 33–66). Springer International Publishing. https://doi.org/10.1007/978-3-319-21386-6_2

Lovett, M., Lee, K., Edwards, A., & Kaplan, D. L. (2009). Vascularization strategies for tissue engineering. *Tissue engineering. Part B, Reviews*, *15*(3), 353–370. https://doi.org/10.1089/ten.TEB.2009.0085

Mabrouk, M., Beherei, H. H., & Das, D. B. (2020). Recent progress in the fabrication techniques of 3D scaffolds for tissue engineering. *Materials Science and Engineering: C*, *110*, 110716. https://doi.org/10.1016/j.msec.2020.110716

Mandrycky, C., Wang, Z., Kim, K., & Kim, D. H. (2016). 3D bioprinting for engineering

complex tissues. In Biotechnology Advances. https://doi.org/10.1016/j.biotechadv.2015.12.011

Markstedt, K., Mantas, A., Tournier, I., Martínez Ávila, H., Hägg, D., & Gatenholm, P. (2015). 3D Bioprinting Human Chondrocytes with Nanocellulose–Alginate Bioink for Cartilage Tissue Engineering Applications. *Biomacromolecules*, *16*(5), 1489–1496. https://doi.org/10.1021/acs.biomac.5b00188

Martinu, T., Pavlisko, E. N., Chen, D. F., & Palmer, S. M. (2011). Acute allograft rejection: cellular and humoral processes. *Clinics in chest medicine*, *32*(2), 295–310.

Min, S., Ko, I. K., & Yoo, J. J. (2019). State-of-the-Art Strategies for the Vascularization of Three-Dimensional Engineered Organs. *Vascular specialist international*, *35*(2), 77–89. https://doi.org/10.5758/vsi.2019.35.2.77

Murphy, S. V., & Atala, A. (2014). 3D bioprinting of tissues and organs. Nature biotechnology, 32(8), 773-785.

Negro, A., Cherbuin, T., & Lutolf, M. P. (2018). 3D Inkjet Printing of Complex, Cell-Laden Hydrogel Structures. *Scientific Reports*, *8*(1), 17099. https://doi.org/10.1038/s41598-018-35504-2

Ong, C. S., Yesantharao, P., Huang, C. Y., Mattson, G., Boktor, J., Fukunishi, T., Zhang, H., & Hibino, N. (2018). 3D bioprinting using stem cells. *Pediatric Research*, *83*(1–2), 223–231. https://doi.org/10.1038/pr.2017.252

Ozbolat, I. (2017). *Extrusion-Based Bioprinting* (pp. 93–124). Pennsylvania State University. https://doi.org/10.1016/B978-0-12-803010-3.00004-4

Pati, F., Jang, J., & Lee, J.-W. (2015). *Extrusion Bioprinting* (pp. 123–152). https://doi.org/10.1016/B978-0-12-800972-7.00007-4

Rouwkema, J., & Khademhosseini, A. (2016). Vascularization and Angiogenesis in Tissue Engineering: Beyond Creating Static Networks. *Trends in Biotechnology*, *34*(9), 733–745. https://doi.org/10.1016/j.tibtech.2016.03.002

Saidi, R. F., & Hejazii Kenari, S. K. (2014). Challenges of organ shortage for transplantation: Solutions and opportunities. *International Journal of Organ Transplantation Medicine*, *5*(3), 87–96.

Shafran, D., Kodish, E., & Tzakis, A. (2014). Organ Shortage: The Greatest Challenge Facing Transplant Medicine. *World Journal of Surgery*, *38*(7), 1650–1657. https://doi.org/10.1007/s00268-014-2639-3

Shi, L., Hu, Y., Ullah, M. W., Ullah, I., Ou, H., Zhang, W., Xiong, L., & Zhang, X. (2019). Cryogenic free-form extrusion bioprinting of decellularized small intestinal submucosa or potential applications in skin tissue engineering. Biofabrication. https://doi.org/10.1088/1758-5090/ab15a9

Skardal, A., Mack, D., Kapetanovic, E., Atala, A., Jackson, J. D., Yoo, J., & Soker, S. (2012). Bioprinted amniotic fluid-derived stem cells accelerate healing of large skin wounds. *Stem Cells Translational Medicine*, *1*(11), 792–802. https://doi.org/10.5966/sctm.2012-0088

Sorkio, A., Koch, L., Koivusalo, L., Deiwick, A., Miettinen, S., Chichkov, B., & Skottman, H.

(2018). Human stem cell based corneal tissue mimicking structures using laser-assisted 3D bioprinting and functional bioinks. *Biomaterials*, *171*, 57–71. https://doi.org/10.1016/j.biomaterials.2018.04.034

Tan, Z., C. Parisi, L. Di Silvio, D. Dini & A. Forte (2017) low 3D Printing of Super Soft Hydrogels. *Scientific Reports,* 7.

Tarassoli, S. P., Jessop, Z. M., Al-Sabah, A., Gao, N., Whitaker, S., Doak, S., & Whitaker, I. S. (2018). Skin tissue engineering using 3D bioprinting: An evolving research field. *Journal of Plastic, Reconstructive & Aesthetic Surgery*, *71*(5), 615–623. https://doi.org/10.1016/j.bjps.2017.12.006

Ukpai, G., & Rubinsky, B. (2020). A three-dimensional model for analysis and control of phase change phenomena during 3D printing of biological tissue. Bioprinting. https://doi.org/10.1016/j.bprint.2020.e00077

Wang, C., Zhao, Q., & Wang, M. (2017). Cryogenic 3D printing for producing hierarchical porous and rhBMP-2-loaded Ca-P/PLLA nanocomposite scaffolds for bone tissue engineering. Biofabrication, 9(2), 025031.

Xia, Z., Jin, S., & Ye, K. (2018). Tissue and Organ 3D Bioprinting. *SLAS TECHNOLOGY: Translating Life Sciences Innovation*, *23*(4), 301–314. https://doi.org/10.1177/2472630318760515

Zhang, X., & Zhang, Y. (2015). Tissue Engineering Applications of Three-Dimensional Bioprinting. *Cell Biochemistry and Biophysics*, *72*(3), 777–782.

https://doi.org/10.1007/s12013-015-0531-x

Zhao, Y., Li, Y., Mao, S., Sun, W., & Yao, R. (2015). The influence of printing parameters on cell survival rate and printability in microextrusion-based 3D cell printing technology. *Biofabrication*, *7*(4), 045002. https://doi.org/10.1088/1758-5090/7/4/045002

Zhu, J., & Marchant, R. E. (2011). Design properties of hydrogel tissue-engineering scaffolds. *Expert review of medical devices*, *8*(5), 607–626. https://doi.org/10.1586/erd.11.27